Journal Name

ARTICLE TYPE

Cite this: DOI: 10.1039/xxxxxxxxxx

Static disorder in a perovskite mixed-valence metal–organic framework†

Ines E. Collings,[a,b*] Paul J. Saines,[c] Mirko Mikolasek,[b] Tiziana Boffa Ballaran,[d] and Michael Hanfland[b]

Received Date
Accepted Date

DOI: 10.1039/xxxxxxxxxx

www.rsc.org/journalname

Variable-temperature and variable-pressure single-crystal diffraction studies are carried out on a mixed-valence perovskite dimethylammonium (DMA) iron formate compound, with the formula $[(DMA_3)(H_2O)][Fe^{II}_3Fe^{III}(HCOO)_{12}]$, in order to investigate potential electric ordering of the DMA cation from its fourfold type of dynamic disorder at ambient conditions. Mössbauer spectroscopy is additionally carried out at ambient conditions to confirm the presence and ratio of Fe^{2+} and Fe^{3+} cations. Below 200 K, a dynamic to static disorder of the DMA cation is observed, while the crystal symmetry and iron formate framework structure remain the same. Upon application of pressure, however, a phase transition occurs that lowers the symmetry above 3.3 GPa. This work highlights the further chemical modifications that are possible within the dimethylammonium metal formates family, *i.e.* doping upon the A-site with neutral molecules, leading to additional opportunities to tune their physical properties.

1 Introduction

Cation-templated metal-formate frameworks show a range of interesting physical properties,[1,2] such as ferroelectricity,[3–7] ferroelasticity,[8] magnetism, and multiferroicity.[9,10] In particular, the optimisation of their multiferroic behaviour would be of great interest for the development of new functional materials.[11] In these compounds, multiferroicity usually arises due to the coexistence and coupling of the magnetic order from the metal–formate framework,[12] and the electric order from the molecular cations in the pores (referred to as A-site cations), through hydrogen bonding interactions.[9] The synthesis of cation-templated metal formates (general formula $A^IM^{II}(HCOO)_3$) is very versatile with structures hosting a range of different A-site and metal cations, as well as dopings on these sites, allowing the physical properties to be tuned.[5,13–17]

Doping and substitutions on the metal cation sites are known for many families of cation-templated metal formates.[13,14,18–26] For instance, dimethylammonium (DMA) iron formates can be synthesised with different iron oxidation state ratios that influence the topologies observed and their physical properties. In particular, they can form in the perovskite (with the Schläfi notation $4^{12}\cdot6^3$),[27] niccolite $(4^9\cdot6^6)(4^{12}\cdot6^3)$,[28] or related $(4^9\cdot6^6)_2(4^{12}\cdot6^3)$ topologies,[29] depending on the ratio of the Fe^{2+} and Fe^{3+} cations. The $[DMA][Fe^{II}(HCOO)_3]$ (DMAFe-1) compound crystallises as colourless cubic crystals with the perovskite structure in $R\bar{3}c$ symmetry,[27] while a combination of Fe^{II} and Fe^{III} yields black crystals of $[DMA][Fe^{II}Fe^{III}(HCOO)_6]$ (DMAFeFe-2) with the $P\bar{3}c$ niccolite structure,[13,28,30,31] or the related $[DMA]_2[Fe^{II}_2Fe^{III}(HCOO)_9]$ (DMAFeFe-3) structure with the $(4^9\cdot6^6)_2(4^{12}\cdot6^3)$ topology in $R\bar{3}c$ symmetry.[29] All three structure types host threefold dynamic disorder of the DMA cations at ambient conditions.[27–29] Upon cooling, the ordering of the DMA cation leads to ferroelectric (at 164 K),[9] or antiferroelectric (at 155 K) transitions[30] for DMAFe-1 and DMAFeFe-2, respectively, while no variable-temperature structural measurements have been performed for DMAFeFe-3. Two recent works report single-crystal diffraction studies on the low-temperature phase of DMAFe-1 that show either a static disorder of the DMA cation with the structure remaining in the average $R\bar{3}c$ symmetry,[32] or an antiferroelectric arrangement of the DMA cations with the $C2/c$ symmetry.[33] The reason for this low-temperature structure discrepancy is not known, but perhaps different cooling rates can affect the final low-temperature structure observed. The weakly ferroelectric behaviour ($P = 0.0018\,\mu C\,cm^{-2}$) observed by pyroelectric measurements[9] suggests that the electric field may be able to induce DMA^+ orien-

[a]Center for X-ray Analytics, Swiss Federal Laboratories for Materials Science and Technology, Überlandstrasse 129, 8600 Dübendorf, Switzerland. E-mail: ines.collings@empa.ch
[b]European Synchrotron Radiation Facility, 38000 Grenoble, France.
[c]School of Physical Sciences, University of Kent, Canterbury, CT2 7NH, U.K.
[d]Bayerisches Geoinstitut, University of Bayreuth, 95447 Bayreuth, Germany.

† Electronic Supplementary Information (ESI) available: Powder diffraction pattern, temperature and pressure dependence of unit cell and polyhedral volumes, reciprocal space reconstruction, and variable-temperature and variable-pressure lattice parameters. The ambient and the variable-temperature $DMAFeFe{\cdot}H_2O$-4 structures have been deposited to the CCDC with the numbers 1979650, and 1990943–1990952, respectively.

tation changes in the static disordered or antiferroelectric low-temperature phase. A disorder–order transition of the DMA cations is known for DMAFeFe-2, giving rise to an antiferroelectric arrangement of DMA^+, accompanied by a tripling of the c-axis and a change of symmetry to $R\bar{3}c$.[30] Additionally, static disorder of the DMA^+ positions along the c-axis was observed.[24] All structures exhibit antiferromagnetic ordering, with small spin canting in DMAFe-1 and DMAFeFe-3 below 20 and 33 K,[29,34] respectively, while DMAFeFe-2 displays ferrimagnetic behaviour below 37 K.[30]

Doping on the A-site cation of metal formates has been less explored, with only two reports known to the best of our knowledge for $[(NH_2NH_3)_x(CH_3NH_3)_{1-x}][Mn(HCOO)_3]$,[15] and $[(NH_3OH)_x(NH_3NH_2)_{1-x}][Zn(HCOO)_3]$.[16] Substitution of the A-site position for neutral molecules, together with the possibility of oxidation on the M site, is a way to vary the doping on both the A-site and the metal cation sites simultaneously, while maintaining the $AM(HCOO)_3$ stoichiometry. This type of A-site substitution was only recently observed during a high-pressure reaction of DMAFeFe-2, yielding the already known DMAFe-1 compound and $[DMA_3][Fe^{II}_3Fe^{III}(HCOO)_{12}]\cdot CO_2$ (DMAFeFe·CO_2-4) or alternatively written as $[(DMA_3)(CO_2)][Fe^{II}_3Fe^{III}(HCOO)_{12}]$ to highlight the positions of the CO_2 molecules on the A-sites.[35] In DMAFeFe·CO_2-4, a quarter of the DMA^+ sites is replaced by CO_2 molecules, and the mixed valence of Fe ensures charge neutrality. It crystallises in cubic symmetry ($Im\bar{3}$) and could be recovered back to ambient conditions. The structure is analogous to the $M^{III}(HCOO)_3$·guest compounds, where M is Mn^{3+}, Fe^{3+}, Al^{3+}, Ga^{3+}, or In^{3+} and the guest molecules are CO_2, H_2O, and HCOOH.[36,37] In this compound, the DMA cation exhibits fourfold dynamic disorder, but no low-temperature or high-pressure studies show its possible ordering, which would be of interest for electric properties optimisation.

Here we investigate the variable-temperature and variable-pressure behaviour of an A-site doped perovskite dimethylammonium iron formate $[DMA_3][Fe^{II}_3Fe^{III}(HCOO)_{12}]\cdot H_2O$ (DMAFeFe·H_2O-4), which can also be written as $[(DMA_3)(H_2O)][Fe^{II}_3Fe^{III}(HCOO)_{12}]$, using single-crystal X-ray diffraction. DMAFeFe·H_2O-4 is structurally analogous to DMAFeFe·CO_2-4, but was synthesised at ambient conditions. In particular, we focus on the possible ordering of the DMA cation from its ambient fourfold type of dynamic disorder. We additionally perform Mössbauer spectroscopy at ambient conditions to confirm the mixed oxidation state of the iron cations.

2 Experimental

2.1 Synthesis

The synthesis of DMAFeFe·H_2O-4 was carried out in two different ways as described below, however, we note that neither synthesis route allowed its synthesis in pure form. In the first synthesis procedure, DMAFeFe·H_2O-4 was formed as an impurity when synthesising DMAFe-1 using old (∼1 year) chemicals. The dimethylammonium iron formate single crystals were grown from slow diffusion methods within a Schlenk tube using the synthesis strategy from Ref. 38. First formic acid (0.094 mL) and dimethylamine (2 M in methanol, 1.25 mL) are mixed with 5 mL of anhydrous methanol, giving a 0.5 M solution and placed at the bottom of the Schlenk tube. Onto this solution, a 0.1 M solution of anhydrous iron(II) chloride (0.1 g) dissolved in 8 mL anhydrous methanol was carefully pipetted. Small crystals would start to grow after a few hours. After a week, the solution was filtered and the crystallites recovered and kept under inert argon atmosphere. From these crystals, a phase mixture was visible due to the different coloured crystals [Figure 1]. Ambient single-crystal X-ray diffraction was performed in order to determine the structure of the dark blue crystals.

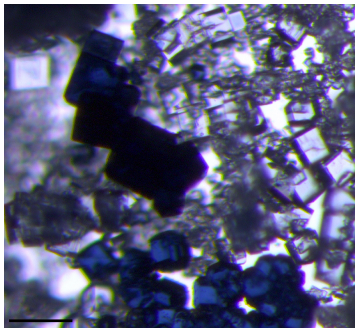

Fig. 1 Microscope image from the synthesis of DMAFe-1 showing clear crystals of DMAFe-1 and dark blue crystals of DMAFeFe·H_2O-4. The black scale bar on the left indicates 100 μm.

In the second synthesis, $FeCl_3$ was additionally used, but the dark blue/black crystals (dark blue is observed for small crystals, while the black colour is prominent for large crystals) formed with an additional orange powder precipitate. In this synthesis, 0.5 mmol of $FeCl_2$ and 0.25 mmol of $FeCl_3\cdot 6H_2O$ were dissolved in 12 mL of MeOH. Onto this solution, a mixture of 1.25 mL dimethylamine and 0.094 mL formic acid in 14 mL of MeOH was added. In this synthesis batch, the crystals had a propensity to display merohedral twinning. The refined crystal structure at ambient conditions gave the same structure as the crystals from the first synthesis batch. From these crystals, variable-temperature and variable-pressure single-crystal diffraction was performed, as well as Mössbauer spectroscopy at ambient conditions.

2.2 Ambient single-crystal X-ray diffraction

Ambient single-crystal diffraction was performed with a single crystal synthesised from batch 1. The crystal was glued on a glass fiber using super glue. Data were collected using an Oxford Diffraction XCalibur diffractometer with Mo wavelength, graphite monochromator, and equipped with a Sapphire2 CCD detector.

2.3 Variable-temperature single-crystal X-ray diffraction

Variable-temperature single-crystal data collections were carried out using a dual source Rigaku Oxford Diffraction Supernova with the Mo-Kα micro-focus source (50 kV, 0.8 mA), with multi-layered focusing optics and an Atlas S2 CCD detector. The crystal was held on a MiTeGen micro loop with oil and cooled with an Oxford Cryosystems cryostream. Data were initially collected at ambient temperature before the crystal was slowly cooled at a rate of 2 K/min to 80 K, where a second measurement was com-

pleted. Data were then measured upon heating up to 160 K, after which the crystal was heated to ambient in order to remove the ice formation. The crystal was then cooled back to 120 K, and data were collected in 20 K steps between 120 K and 300 K, with an equilibration time for each step of 5 minutes before data collection commenced. Heating and cooling rates following the initial cooling used the standard 6 K/min rate.

2.4 High-pressure single-crystal X-ray diffraction

High-pressure (HP) single-crystal X-ray diffraction on DMAFeFe·H_2O-4 was measured at the ID15B beamline of the European Synchrotron Radiation Facility, Grenoble up to 4.6 GPa using monochromatic X-ray radiation ($\lambda = 0.411110$ Å). Membrane driven LeToullec type diamond anvil cells (DACs) were used, equipped with Boehler-Almax anvils. Stainless steel was used as the gasket material, and neon was loaded as the pressure-transmitting medium. Diffraction patterns were collected with a Mar555 flat panel detector using steps of 0.5° oscillations over a total ω scan range of 76° about the vertical axis. The pressures were measured using the ruby fluorescence method before and after each diffraction measurement. The average of both pressure values was used and the variance was employed to estimate the errors associated with the pressure measurement, in addition to the ±0.05 GPa error to account for the error in the ruby florescence method in the pressure range below 10 GPa.[39]

2.5 Single-crystal data solution and refinement

Lattice parameter determination and integration of the reflection intensities were performed using the *CrysAlisPro* software.[40] Structure solution was performed using SHELXT and subsequent least-squares refinements were carried out using SHELXL within the ShelXle graphical user interface.[41–43] For the ambient single-crystal data collection, the atomic positions were refined freely for all atoms apart from the H atom of the formate anion, which was refined using geometric and distance constraints. The H atoms from the DMA cation have distance restraints in place as well as the thermal parameters 1.2 times that of the C and N atoms. Isotropic thermal parameters were refined for all hydrogen atoms, the oxygen from the disordered water molecule, and the N site that is split into two along the C–N–C bonding direction. The thermal parameters of all other atoms were refined anisotropically. A similar procedure was adopted for the variable-temperature and pressure data sets, but due to reduced number of reflections, no H atoms were placed on the DMA cation, nor on the oxygen of the disordered water (for the HP data) in order to restrict the number of refinable parameters. In addition, isotropic thermal parameters were employed for both symmetry-inequivalent N sites, and no additional N split along the C–N–C bonding direction was modelled (*i.e.* all N atoms of the DMA cation were at 0.25 occupancy).

The refinements at different temperatures and pressures used the structural model from the previous temperature or pressure point as a starting model for refinement.

2.6 Mössbauer spectroscopy

Mössbauer measurements were carried out at the nuclear resonance beamline ID18 at the ESRF using synchrotron Mössbauer spectroscopy (SMS).[44,45] In this experiment, crystallites were placed within a hole drilled in a kapton sheet with the thickness of 200 μm. The beam of γ-radiation emitted by the SMS was focused to a 10 μm × 15 μm spot size, and the velocity scales of all SMS were calibrated relative to 25 μm-thick α-Fe foil. Three measurements were performed on different positions of the sample and summed together. The summed data were fitted using the software package MossA.[46]

3 Results

3.1 Ambient structure

The crystal structure of DMAFeFe·H_2O-4 contains iron octahedra connected through formate ligands giving an extended three-dimensional structure with the ReO_3 topology [Figure 2]. The FeO_6 octahedra are tilted in phase, giving it the Glazer tilt notation of $a^+a^+a^+$.[47] Three-quarters of the pores are filled with DMA cations, while the other quarter is filled with water molecules. The DMA cations exhibit a dynamic disorder of the NH_2 group into four overall main sites perpendicular to the C–N–C bonding, with additionally two symmetry-related N positions splitting in two along the C–N–C bonding direction [Figure 2(b)]. This highlights movement along the C–N–C bonding direction, also observed in the large thermal parameters for the other non-

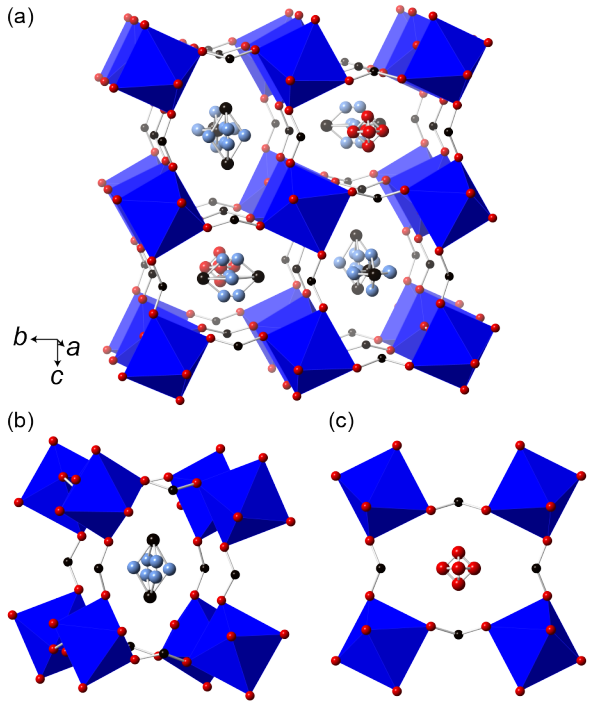

Fig. 2 (a) Ambient structure of DMAFeFeF·H_2O-4 with disordered DMA cations in three-quarters of the pores and H_2O in the remaining quarter of the pores. Insets of the pores with the disordered (b) DMA cation and (c) water are also shown. Iron octahedra are shown as filled blue polyhedra. Atom colours represent C for black, O for red, and N for light blue. The hydrogen atoms have been omitted for clarity.

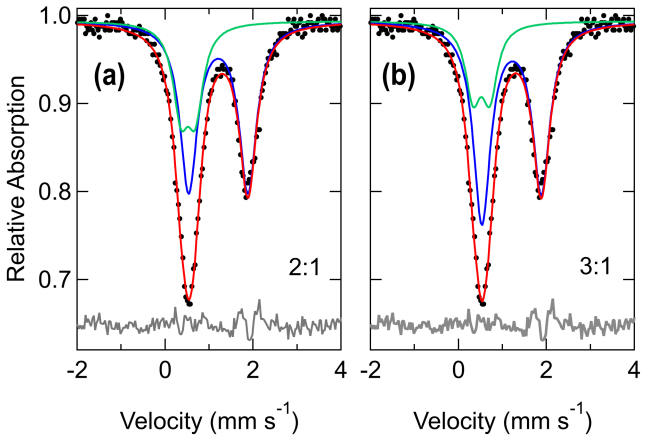

Fig. 3 Mössbauer spectrum of DMAFeFe·H_2O-4 with (a) the area ratios of Fe^{2+}/Fe^{3+} freely refined and (b) a 3:1 ratio imposed and the additional refinement of the area doublet ratio for the Fe^{2+}. The black points represent the data, the blue and green subspectra indicate the Fe^{2+} and Fe^{3+} sites, respectively, the red line is the total fit, and the grey line is the residual, moved up vertically for easier view.

split N and C sites of the DMA cation. Due to the complexity in this disorder, we assume that the two symmetry inequivalent N sites have a quarter occupancy (which is further reduced to one-eighth in the case of the split N). This disorder contrasts with the threefold disorder observed in the related DMAFe-1, DMAFeFe-2, and DMAFeFe-3 compounds.[27–29] In order to counterbalance the charge in the structure, a mixture of Fe^{2+} and Fe^{3+} cations is needed. Crystallographically, only one unique Fe site is present, and so the distribution of Fe^{2+} and Fe^{3+} cations is randomly arranged throughout the structure. In our model, the DMA cations and water molecules are fully occupied in their sites, giving the overall unit cell formula as $[DMA_6][Fe^{II}_6Fe^{III}_2(HCOO)_{24}]\cdot 2H_2O$, or $[DMA_{0.75}][Fe^{II}_{0.75}Fe^{III}_{0.25}(HCOO)_3]\cdot 0.25H_2O$ as the chemical formula unit, which gives a 3:1 ratio of Fe^{2+}/Fe^{3+} based upon charge balance.

Recently, the analogous structure DMAFeFe·CO_2-4 was synthesised at high pressure from the starting crystal DMAFeFe-2 when pressurised in a MeOH:EtOH mixture.[35] The HP structure could be recovered to ambient conditions, and its cubic lattice parameter was refined as 12.0752(4) Å.[35] In our structures, a slightly smaller lattice parameter is observed at 12.04747(16) Å, and the position for the disordered neutral guest could be better modelled as a water molecule [Figure 2(c)]. The presence of water as the guest species upon ambient synthesis conditions may be more reasonable considering that the CO_2 formed from the decomposition of formic acid or formate would be released from the solution state, while during the *in-situ* formation in the DAC, the CO_2 is kept within the sample chamber.

Mössbauer spectroscopy was used to confirm the presence and relative ratios of Fe^{2+} and Fe^{3+}. Prior to the Mössbauer measurement, a diffraction pattern was measured on the same sample to check purity and any preferred orientation effects (Figure S1(a)). While the diffraction pattern showed a phase pure sample, there was a slight mismatch in the intensities, which could be better modelled with preferred orientation parameters (Figure S1(b,c)). The preferred orientation will have an impact on the refined Fe^{2+}/Fe^{3+} ratios and so two fits of the Mössbauer spectrum were performed, illustrated in Figure 3. The first fit shows a freely refined Fe^{2+}/Fe^{3+} ratio and indicates the presence of 69% Fe^{2+} and 31% Fe^{3+} cations, giving a ratio close to 2:1 [Figure 3(a), Table 1]. In the second fit, the Fe^{2+}/Fe^{3+} ratio was fixed at 3:1, and the area doublet of the Fe^{2+} was allowed to refine to account for preferred orientation effects [Figure 3(b), Table 1]. Both refinement strategies fit equally well the data, and so we keep the structural model with a 3:1 Fe^{2+}/Fe^{3+} ratio that is consistent with the single-crystal data.

Table 1 Isomer shift (IS), quadrupole splitting (QS), relative areas of the Fe^{2+} and Fe^{3+} sites, and the full-width half-maximum (FWHM) determined from Mössbauer data for both the freely refined Fe^{2+}/Fe^{3+} ratio (Figure 3(a)) and the fixed 3:1 Fe^{2+}/Fe^{3+} ratio (Figure 3(b)) with the area doublet ratio of the Fe^{2+} refined to 0.542(10) (instead of the usual 0.5 doublet area ratio).

site	IS ($mm\,s^{-1}$)	QS ($mm\,s^{-1}$)	area (%)	FWHM
Fe^{2+}	1.208(6)	1.348(12)	69.0(14)	0.48(2)
Fe^{3+}	0.520(15)	0.33(3)	31.0(14)	0.43(4)
Fe^{2+}	1.207(5)	1.349(10)	75	0.47(2)
Fe^{3+}	0.519(15)	0.38(4)	25	0.42(2)

4 Variable-temperature diffraction

The single crystals of DMAFeFe·H_2O-4 used for the variable-temperature diffraction exhibited merohedral twinning with the twin law [0 1 0, 1 0 0, 0 0 −1], as determined using XPREP.[48] The crystal was first cooled to 80 K and data were collected upon heating back to 300 K. Figure 4(a) shows the evolution of the cubic *a*-lattice parameter as a function of temperature, where a discontinuity can be observed between 180 and 200 K. No change in the crystal symmetry and overall structure could be observed. The expansion of the crystal with temperature is mainly dic-

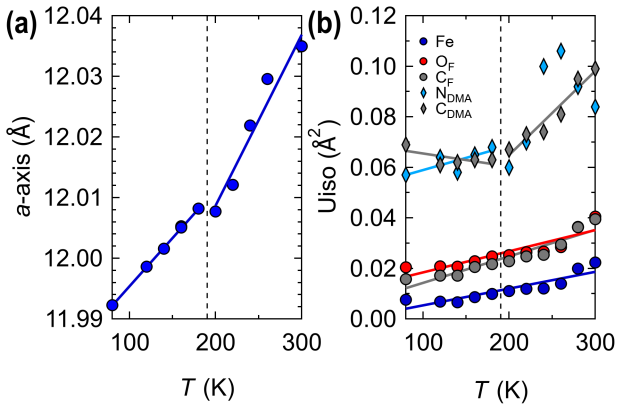

Fig. 4 (a) Cubic lattice parameter as a function of temperature. (b) Equivalent isotropic thermal parameters as a function of temperature for Fe, O_F and C_F from the formate anion, and N_{DMA}, C_{DMA} from the DMA cation. The dotted black line suggests the transition temperature upon heating for the static to dynamic disorder of the DMA cation.

tated by the changes in the polyhedral volume of FeO_6 [Figure S2], with the volume expansivity of the unit cell calculated as $\alpha_V = \frac{1}{V}\frac{dV}{dT} = 52(3)\,MK^{-1}$ while that of the octahedral volume is $\alpha_{V\,oct} = 51(8)\,MK^{-1}$, as calculated using the web tool PASCal.[49]

The thermal parameters of the iron, formate ligands and DMA cation highlight some differences in temperature variation. In particular, a continuous increase for the iron and formate ions is observed upon heating, while the C and N atoms from the DMA cation exhibit a discontinuity at 180–200 K [Figure 4(b)]. Specifically, their thermal parameters remain roughly constant from 80 to 180 K, and begin to increase above 200 K. This behaviour could indicate a static to dynamic disorder of the DMA cations upon heating. The dynamic–static transition of DMA cations is also observed for DMAFe-1,[32] $[DMA][Fe^{III}M^{II}(HCOO)_6]$ where M = Zn^{2+}, Ni^{2+}, Mg^{2+},[18,31] and $[DMA][Ga^{III}M^{II}(HCOO)_6]$ for M = Fe^{2+}, Ni^{2+}.[25]

5 High-pressure diffraction

Three single crystals of DMAFeFe·H_2O-4 were loaded in the sample chamber of a diamond anvil cell with neon as the pressure-transmitting medium. Previous studies on similar materials have shown that increasing exposure to the X-ray beam can inhibit phase transition behaviour,[50,51] thus several crystals were loaded for this reason. The crystal measured up to 4.4 GPa was stable in the ambient phase although it exhibited a loss in resolution and peak broadening above 3.3 GPa [Figure 5]. A second crystal within the sample chamber (only exposed to X-ray radiation at ambient pressure for the quality check of the crystal, see Figure S4) displayed in addition to a loss in resolution and peak broadening, the appearance of a lower-symmetry phase in coexistence with the cubic phase [Figure 5]. Due to the low intensity and resolution, broad peaks, and twinning of this new phase, we could not index it. We note that even with ordered guests, there is not sufficient space for incorporation of neon into the structure, so it is unlikely that Ne participates in the phase transition behaviour, or promotes a chemical reaction due to its inert nature.

The volume–pressure dependence is shown in Figure 6. A second-order Birch-Murnaghan equation of state was fitted up to 3.3 GPa using PASCal[49] yielding the bulk modulus of B_0 = 28.4(3) GPa and the calculated volume at ambient pressure of V_0 = 1745.5(10) Å^3, close to the experimentally observed volume at 1744.0(4) Å^3. The B_0 value is similar to the one determined for DMAFe-1 at 27.2(7) GPa.[50] However, the onset of a phase transition is much lower in DMAFeFe·H_2O-4 compared to DMAFe-1 (3.8(6) GPa *vs* 7.3(2) GPa). This most likely arises from the 25% of cavities being filled with neutral water instead of being fully occupied with DMA cations as is the case in DMAFe-1.

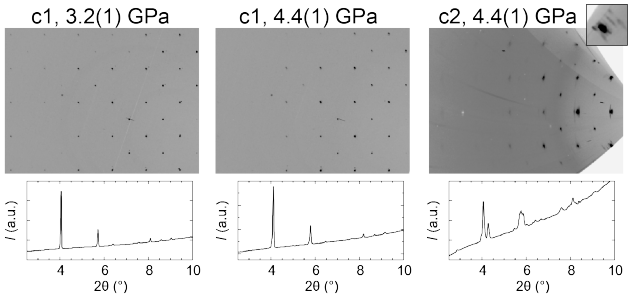

Fig. 5 (*Top*) Reciprocal space reconstructions for crystal 1 and crystal 2, highlighting the coexistence of the high-pressure and ambient phases in crystal 2 and loss of resolution in crystal 1. An inset for crystal 2 highlights the main broad cubic reflection, surrounded by weaker diffraction spots from the lower-symmetry phase. (*Bottom*) Powder diffraction patterns extracted from the wide image scans (±20° continuous scan).

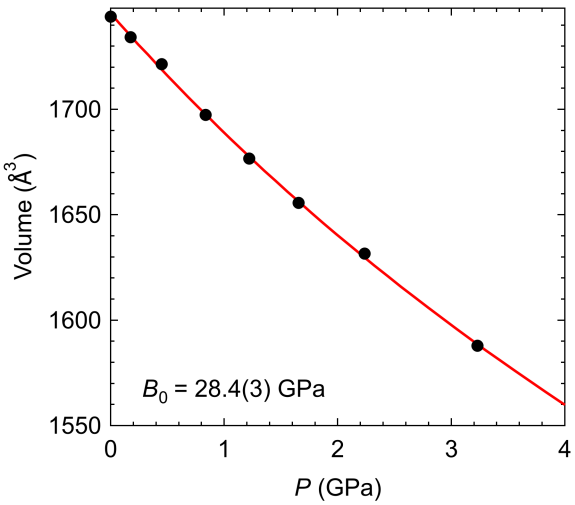

Fig. 6 Pressure dependence of the crystal 1 volume with the second order Birch-Murnaghan fit shown in solid red line.

The pressure dependence of the unit cell volume is greater than that of the octahedral FeO_6 volume [Figure S3], indicating that the compression of DMAFeFe·H_2O-4 arises not only from FeO_6 octahedral volume reduction but also from other compression mechanisms, such as octahedral tilting.

6 Conclusions

We have synthesised a filled ReO_3 iron formate framework through incorporation of DMA cations and water in the pores (A-site position) and by use of mixed oxidation states of Fe cations. The ratio and presence of both Fe^{2+} and Fe^{3+} are shown with single-crystal diffraction studies and Mössbauer spectroscopy as 3:1, giving the formula as $[(DMA_3)(H_2O)][Fe^{II}_3Fe^{III}(HCOO)_{12}]$. This structure yields a fourfold type disorder of the DMA cations, as has also been found in the analogous compound with CO_2 instead of H_2O as neutral guests. The variable-temperature single-crystal diffraction data suggest a dynamic to static disorder change in the DMA cations below 200 K. The variation in the Fe^{2+}/Fe^{3+} ratio allows a direct access to the filling of the pores with neutral guests or charged molecular cations, that could allow a way to tune certain physical properties and porosities through removal of the neutral guest.

Conflicts of interest

There are no conflicts to declare.

Acknowledgement

We acknowledge the European Synchrotron Radiation Facility for the provision of beamtime on ID18 (Mössbauer data) and ID15B (high-pressure single-crystal diffraction data). P.J.S thanks the EPSRC for funding as part of the grant EP/R011524/1. We thank V. Cerantola, J.-P. Celse, and A. Chumakov for their assistance with the setup of the Mössbauer measurements.

References

1 L.-H. Chen, J.-B. Guo, X. Wang, X.-W. Dong, H.-X. Zhao, L.-S. Long and L.-S. Zheng, *Adv. Mater.*, 2017, **29**, 1702512.

2 J.-P. Zhao, S.-D. Han, X. Jiang, S.-J. Liu, R. Zhao, Z. Chang and X.-H. Bu, *Chem. Commun.*, 2015, **51**, 8288–8291.

3 G.-C. Xu, X.-M. Ma, L. Zhang, Z.-M. Wang and S. Gao, *J. Am. Chem. Soc.*, 2010, **132**, 9588–9590.

4 G.-C. Xu, W. Zhang, X.-M. Ma, Y.-H. Chen, L. Zhang, H.-L. Cai, Z.-M. Wang, R.-G. Xiong and S. Gao, *J. Am. Chem. Soc.*, 2011, **133**, 14948–14951.

5 D. Di Sante, A. Stroppa, P. Jain and S. Picozzi, *J. Am. Chem. Soc.*, 2013, **135**, 18126–18130.

6 P. Jain, A. Stroppa, D. Nabok, A. Marino, A. Rubano, D. Paparo, M. Matsubara, H. Nakotte, M. Fiebig, S. Picozzi *et al.*, *npj Quantum Mater.*, 2016, **1**, 16012.

7 A. Sieradzki, M. Mączka, M. Simenas, J. K. Zaręba, A. Gągor, S. Balciunas, M. Kinka, A. Ciupa, M. Nyk, V. Samulionis, J. Banys, M. Paluch and S. Pawlus, *J. Mater. Chem. C*, 2018, **6**, 9420–9429.

8 W. Li, Z. Zhang, E. G. Bithell, A. S. Batsanov, P. T. Barton, P. J. Saines, P. Jain, C. J. Howard, M. A. Carpenter and A. K. Cheetham, *Acta Mater.*, 2013, **61**, 4928–4938.

9 Y. Tian, A. Stroppa, Y. Chai, L. Yan, S. Wang, P. Barone, S. Picozzi and Y. Sun, *Sci. Rep.*, 2014, **4**, 6062.

10 L. C. Gómez-Aguirre, B. Pato-Doldán, J. Mira, S. Castro-García, M. A. Señarís-Rodríguez, M. Sánchez-Andújar, J. Singleton and V. S. Zapf, *J. Am. Chem. Soc.*, 2015, **138**, 1122–1125.

11 G. Rogez, N. Viart and M. Drillon, *Angew. Chem. Int. Ed.*, 2010, **49**, 1921–1923.

12 Z. Wang, K. Hu, S. Gao and H. Kobayashi, *Adv. Mater.*, 2010, **22**, 1526–1533.

13 J.-P. Zhao, B.-W. Hu, F. Lloret, J. Tao, Q. Yang, X.-F. Zhang and X.-H. Bu, *Inorg Chem*, 2010, **49**, 10390–10399.

14 M. Mączka, A. Sieradzki, B. Bondzior, P. Dereń, J. Hanuza and K. Hermanowicz, *J. Mater. Chem. C*, 2015, **3**, 9337–9345.

15 S. Chen, R. Shang, B.-W. Wang, Z.-M. Wang and S. Gao, *Angew. Chem. Int. Ed.*, 2015, **54**, 11093–11096.

16 G. Kieslich, S. Kumagai, A. C. Forse, S. Sun, S. Henke, M. Yamashita, C. P. Grey and A. K. Cheetham, *Chem Sci*, 2016, **7**, 5108–5112.

17 J.-P. Zhao, S.-D. Han and F.-C. Liu, *Inorg Chem*, 2019, **58**, 1184–1190.

18 A. Ciupa, M. Mączka, A. Gągor, A. Pikul and M. Ptak, *Dalton Trans.*, 2015, **44**, 13234–13241.

19 N. L. Evans, P. M. M. Thygesen, H. L. B. Boström, E. M. Reynolds, I. E. Collings, A. E. Phillips and A. L. Goodwin, *J. Am. Chem. Soc.*, 2016, **138**, 9393–9396.

20 M. Mączka, A. Ciupa, A. Gągor, A. Sieradzki, A. Pikul and M. Ptak, *J. Mater. Chem. C*, 2016, **4**, 1186–1193.

21 M. Mączka, A. Gągor, K. Hermanowicz, A. Sieradzki, L. Macalik and A. Pikul, *J. Solid State Chem.*, 2016, **237**, 150 – 158.

22 M. Ptak, M. Mączka, A. Gągor, A. Sieradzki, B. Bondzior, P. Dereń and S. Pawlus, *Phys. Chem. Chem. Phys.*, 2016, **18**, 29629–29640.

23 M. Ptak, M. Mączka, A. Gągor, A. Sieradzki, A. Stroppa, D. Di Sante, J. M. Perez-Mato and L. Macalik, *Dalton Trans.*, 2016, **45**, 2574–2583.

24 A. Sieradzki, S. Pawlus, S. Tripathy, A. Gągor, A. Ciupa, M. Mączka and M. Paluch, *Phys. Chem. Chem. Phys.*, 2016, **18**, 8462–8467.

25 K. Wang, J.-B. Xiong, B. Xia, Q.-L. Wang, Y.-Z. Tong, Y. Ma, Z.-M. Wang and S. Gao, *Inorg Chem*, 2018, **57**, 3941–3947.

26 H. L. Boström, J. Bruckmoser and A. L. Goodwin, *J. Am. Chem. Soc.*, 2019, **141**, 17978–17982.

27 P. Jain, V. Ramachandran, R. J. Clark, H. D. Zhou, B. H. Toby, N. S. Dalal, H. W. Kroto and A. K. Cheetham, *J. Am. Chem. Soc.*, 2009, **131**, 13625–13627.

28 K. S. Hagen, S. G. Naik, B. H. Huynh, A. Masello and G. Christou, *J. Am. Chem. Soc.*, 2009, **131**, 7516–7517.

29 K.-H. Jin, S.-Y. Wang, K. Wang, B. Xia, Y.-Z. Tong, Y. Ma and Q.-L. Wang, *Inorg. Chem. Commun.*, 2019, **105**, 26 – 30.

30 L. Cañadillas-Delgado, O. Fabelo, J. A. Rodríguez-Velamazán, M.-H. Lemée-Cailleau, S. A. Mason, E. Pardo, F. Lloret, J.-P. Zhao, X.-H. Bu, V. Simonet, C. V. Colin and J. Rodríguez-Carvajal, *J. Am. Chem. Soc.*, 2012, **134**, 19772–19781.

31 A. Ciupa, M. Mączka, A. Gągor, A. Sieradzki, J. Trzmiel, A. Pikul and M. Ptak, *Dalton Trans.*, 2015, **44**, 8846–8854.

32 I. E. Collings, D. M. Vasiukov, C. A. McCammon, L. Dubrovinsky, V. Cerantola, S. Petitgirard, C. B. Hübschle, A. Schönleber, D. Chernyshov, S. van Smaalen and N. Dubrovinskaia, *J. Phys. Chem. C*, 2019, **123**, 21676–21684.

33 Y. Ma, Y. Wang, J. Cong and Y. Sun, *Phys. Rev. Lett.*, 2019, **122**, 255701.

34 Y. Tian, W. Wang, Y. Chai, J. Cong, S. Shen, L. Yan, S. Wang, X. Han and Y. Sun, *Phys. Rev. Lett.*, 2014, **112**, 017202.

35 S. Sobczak and A. Katrusiak, *Inorg. Chem.*, 2019, **58**, 11773–11781.

36 A. Cornia, A. Caneschi, P. Dapporto, A. C. Fabretti, D. Gatteschi, W. Malavasi, C. Sangregorio and R. Sessoli, *Angew. Chem. Int. Ed.*, 1999, **38**, 1780–1782.

37 Y.-Q. Tian, Y.-M. Zhao, H.-J. Xu and C.-Y. Chi, *Inorg Chem*, 2007, **46**, 1612–1616.

38 Z. Wang, B. Zhang, T. Otsuka, K. Inoue, H. Kobayashi and M. Kurmoo, *Dalton Trans.*, 2004, 2209–2216.

39 J. M. Recio, J. M. Menéndez and A. O. de la Roza, *An Introduction to High-Pressure Science and Technology*, CRC Press, 2016.

40 *Rigaku Oxford Diffraction, (2018), CrysAlisPro Software system, version 1.171.38.46, Rigaku Corporation, Oxford, UK.*

41 G. M. Sheldrick, *Acta Cryst. A*, 2015, **71**, 3–8.

42 G. Sheldrick, *Acta Cryst. A*, 2008, **64**, 112–122.

43 C. B. Hübschle, G. M. Sheldrick and B. Dittrich, *J. Appl. Crystallogr.*, 2011, **44**, 1281–1284.

44 R. Rüffer and A. I. Chumakov, *Hyperfine Interact.*, 1996, **97**, 589–604.

45 V. Potapkin, A. I. Chumakov, G. V. Smirnov, J.-P. Celse, R. Rüffer, C. McCammon and L. Dubrovinsky, *J. Synchrotron Rad.*, 2012, **19**, 559–569.

46 C. Prescher, C. McCammon and L. Dubrovinsky, *J. Appl. Crystallogr.*, 2012, **45**, 329–331.

47 A. Glazer, *Acta Cryst. B*, 1972, **28**, 3384–3392.

48 XPREP, *X-ray data Preparation and Reciprocal space Exploration Program*, Bruker axs inc., madison, wisconsin, usa. technical report, 2014.

49 M. J. Cliffe and A. L. Goodwin, *J. Appl. Cryst.*, 2012, **45**, 1321–1329.

50 I. E. Collings, M. Bykov, E. Bykova, M. Hanfland, S. van Smaalen, L. Dubrovinsky and N. Dubrovinskaia, *CrystEngComm*, 2018, **20**, 3512–3521.

51 H. L. Boström, I. E. Collings, A. B. Cairns, C. P. Romao and A. L. Goodwin, *Dalton Trans.*, 2019, **48**, 1647–1655.